Water Resources Research

RESEARCH ARTICLE
10.1029/2019WR025960

Patch-Based Multiscale Algorithm for Flow and Reactive Transport in Fracture-Microcrack Systems in Shales

Ziyan Wang[1] and Ilenia Battiato[1]

[1]Department of Energy Resources Engineering, Stanford University, Stanford, CA, USA

Key Points:
- We develop a fully coupled patch-based multiscale algorithm, which allows us to model reactive transport in fracture-microcrack systems
- The patch-based algorithm can model the reactive transport with microcrack clogging, which cannot be solved by upscaling methods
- The speedup of the patch-based simulation (without parallel computation) is about 10-fold compared to the fully resolved simulation

Correspondence to:
I. Battiato,
ibattiat@stanford.edu

Citation:
Wang, Z., & Battiato, I. (2020). Patch-based multiscale algorithm for flow and reactive transport in fracture-microcrack systems in shales. *Water Resources Research*, *56*, e2019WR025960. https://doi.org/10.1029/2019WR025960

Received 9 JUL 2019
Accepted 2 DEC 2019
Accepted article online 7 JAN 2020

Abstract A major challenge in modeling reactive transport in shales is the multiscale nature of the fractured rock system. Shales may contain a few main fractures and thousands of microcracks whose length and aperture are orders of magnitude smaller than the former. This renders fully resolved simulations too expensive, while traditional upscaling methods cannot accurately capture fracture clogging dynamics due to precipitation. We develop a fully coupled patch-based multiscale algorithm to address this issue: We solve reactive transport only in a few selected microcracks, while evaluating the others by interpolation and ensuring top-down bottom-up coupling between the main fracture and the microcracks. Specifically, we consider a fracture system with an array of hundreds of microcracks connected to a main fracture. The patch-based multiscale algorithm is validated against fully resolved pore-scale simulations and a steady-state analytical solution. We find the reaction rate can have a great impact on the concentration profiles after breakthrough, even if the profiles before breakthrough are similar. Also, the breakthrough curves exhibit three dynamic regimes when microcrack aperture alterations are accounted for.

1. Introduction

The production of unconventional hydrocarbons has been growing rapidly in recent years, making it possible for the United States and other regions to reduce energy imports and even become energy independent (Sakmar, 2011; Vidic et al., 2013). Unconventional hydrocarbons refer to the gas and oil stored in ultrafine-grained rocks (collectively referred to as shales). Due to the extremely low permeability of shales, the formation needs to be fractured before hydrocarbons can be produced. Mostly, the fracturing is accomplished by injecting a large amount of water (about 15,000 m^3 per well) into the formation at high pressure (i.e., hydraulic fracturing) (Torres et al., 2016). Because of the huge water consumption, the rapid expansion of unconventional gas and oil production poses a threat to water resources (Entrekin et al., 2011). It is estimated that 31–44% of shale deposits are located in areas where water stress will limit the production (Rosa et al., 2018). Another risk is the disposal of the flowback and produced water (collectively referred to as wastewater) from the hydraulic fracturing operations, which contains toxic chemicals and natural radioactive materials and thus cannot be disposed of normally (Entrekin et al., 2011; Liden et al., 2017). In many states (e.g., Texas), most wastewater is injected into deep wells for disposal, but recent research shows that the injection may cause ground water contamination and induced seismicity (Ellsworth, 2013; Torres et al., 2016; Vengosh et al., 2014).

Currently, one of the most promising technologies to curb such impacts is reusing the wastewater in subsequent hydraulic fracturing operations (Gregory et al., 2011). In Pennsylvania, over 90% of wastewater is already reused directly or after dilution or pretreatment (Maloney & Yoxtheimer, 2012). However, operators hold different opinions about the quality of wastewater that must be achieved for reuse (Vidic et al., 2013). One major concern is the precipitation (mainly $BaSO_4$) in shale formations that may block the pathways for gas and oil recovery (Paukert Vankeuren et al., 2017; Vidic et al., 2013). Recent experiments show that the fracking fluid can be imbibed into shales through microcracks and react with minerals, causing precipitation or dissolution (Alalli et al., 2018; Li et al., 2018). Precipitation may clog the microcracks, which offer pathways for the gas transport from the porous matrix to the hydraulic fractures, while dissolution may increase the fracture conductivity (Alalli et al., 2018; Li et al., 2018). Reactive transport modeling can help to evaluate the impact of mineral reactions on well productivity and determine the minimum treatment for the wastewater, optimizing hydraulic fracturing operations.

Since, due to the extremely low permeability of shale matrix, most permeability is contributed by the fractures, modeling reactive transport in the fracture network of shales is paramount to achieve accurate predictions of mass transport and reactions. Generally, the fracture network contains three types of fractures: hydraulic fractures, natural fractures, and microcracks. Hydraulic fractures are the fractures created by injecting high-pressure water into the formation. They are major pathways for hydrocarbon recovery, whose aperture is a few millimeters. Natural fractures are fractures preexisting hydraulic fracturing operations with apertures ranging from tens of micrometers to a few millimeters. Microcracks are the fractures with an aperture from a few micrometers to tens of micrometers. They can be naturally present or induced by stress changes (e.g., during drilling or hydraulic fracturing).

A major challenge in modeling flow and transport in shales stems from the multiscale nature of the fracture network. The aperture (and length) of microcracks is much smaller than those of hydraulic fractures and natural fractures, while their density is much larger (Middleton et al., 2015). Thus, a rock system that contains a few main fractures may have thousands of microcracks. At small scales, experiments have demonstrated how microcracks can be entirely clogged by precipitates (Alalli et al., 2018), and pore-scale simulations have revealed aperture alterations in single fractures (Li et al., 2008) and submillimeter fracture networks in shales (Soulaine & Tchelepi, 2016). At large scales, even state-of-the-art discrete fracture network models, which can simulate flow and transport in complex 3-D fracture networks (Hyman et al., 2015; Karra et al., 2015), become computationally prohibitive if main fractures are to be explicitly resolved together with all associated microcracks. Therefore, a multiscale approach, able to capture the impact that small-scale features have at a large scale, is desired.

One traditional approach is to model small-scale features (e.g., the microcracks) as an effective medium. Upscaling methods, routinely used in a variety of disciplines ranging from single (Heße et al., 2009; Li et al., 2006; Moslehi et al., 2016; Orgogozo et al., 2010) and multiphase flow in natural porous media (Picchi & Battiato, 2018, 2019; Picchi et al., 2018) to food science (Takhar et al., 2011) and electrochemical storage (Arunachalam et al., 2015), allow one to formally derive continuum-scale equations whose effective coefficients are obtained by solving a closure problem at the microscale. A review of a number of upscaling tools, as well as their advantages and drawbacks, is given by Battiato et al. (2019). Regardless the specific upscaling method employed, limitations exist about the applicability of continuum-scale models (Battiato & Tartakovsky, 2011; Battiato et al., 2019; Boso & Battiato, 2013; Korneev & Battiato, 2016). While the fracture-matrix conceptualization allows one to significantly reduce the problem complexity (Dejam et al., 2014; Ling et al., 2016, 2018; Roubinet et al., 2012), there are classes of physical processes that do not lend themselves to accurate macroscopic descriptions (e.g., when the microcracks are fully clogged). Multiscale hybrid methods, in which two or more models at different scales are directly coupled in a single simulation, represent a computationally efficient alternative to fully resolved simulations since they resolve a high-fidelity model (e.g., pore scale) only in a small portion of the computational domain and couple it to an effective medium model everywhere else. The coupling can be performed by using either monolithic or domain-decomposition methods. Monolithic (a.k.a. intrusive) approaches are based on overlapping domains (e.g., pore and continuum scale) and build the coupling through a single discrete multiscale operator (Battiato et al., 2011; Roubinet & Tartakovsky, 2013). Instead, in hybrid algorithms based on domain-decomposition (or nonintrusive) methods, the coupling between adjacent domains at different scales is enforced through multiscale boundary conditions. A large number of approaches have been proposed based on finite volumes (Balhoff et al., 2007; Yousefzadeh & Battiato, 2017), Smoothed Particle Hydrodynamics (Tartakovsky et al., 2008), multiscale mortar finite elements (Arbogast et al., 2007), and Pore-Network-Models (Balhoff et al., 2007; Mehmani & Balhoff, 2014; Mehmani et al., 2012) in the context of mortar methods (Balhoff et al., 2008; Peszyńska et al., 2002), just to mention a few. Yet the fundamental hypothesis underlying such methods is that the portion of the domain in which high-fidelity models are needed be much smaller than the computational domain. From this point of view, shales present unique challenges since the fine-scale features; that is, microcracks, where critical processes occur, occupy the entire macroscopic domain. As a result, the numerical study of flow and transport in shales has been far more scarce compared to other types of natural porous media.

Patch dynamics methods have been used in applications where a given detailed microscopic simulator needs to be employed over macroscopic scales and constitutive laws are not available. The equation free method adopts a bottom-up approach, in which the macroscale solution is constructed based on microscale

simulations in small patches. A review of the method is provided in Samaey et al. (2010). The heterogeneous multiscale method, on the other hand, employs a top-down algorithm. It starts with an incomplete macroscale model, while using an microscale model as a supplement (Weinan et al., 2007). Here, we develop an iterative bottom-up top-down patch-based interpolation scheme to model flow and reactive transport in shales while accounting for their multiscale nature. In this approach, two simulation domains are identified: The first is characterized by larger characteristic length scales where macroscale models or a lower numerical resolution can be employed, and the second where microscale models or higher numerical resolution is necessary. Small sampling regions (i.e., patches) are defined in the latter simulation domain and solved by fine-scale simulations, while the gaps between sampling regions are evaluated by interpolation. Since the fine-scale simulations are only performed in the sampling regions, which only occupy a small portion of the entire computational domain, the computational burden of solving fine-scale problems over macroscopic length scales can be controlled (Wang et al., 2016, 2018). Differently from the original adoption of patch-based interpolation in the context of equation free methods where the coupling between the macroscales and microscales is bottom-up (Gear et al., 2003; Kevrekidis et al., 2004), the proposed algorithm is based on a bottom-up top-down coupling where the boundary condition between the two simulation domains is updated iteratively. While applicable to complex patterns, the multiscale algorithm is demonstrated on a system where an array of microcracks is connected to a main fracture. First, the algorithm is validated against fully resolved pore-scale simulations under different conditions as well as a steady-state analytical solution and then generalized to model microcracks clogging due to localized precipitation.

The manuscript is organized as follows. In sections 2 and 3, we present the physical model and the multiscale algorithm, respectively. Section 4 contains the algorithm validation and its application to reactive transport with and without microcrack geometry alterations. We summarize the major conclusions of this work in section 5.

2. Physical Model

We consider flow of an incompressible Newtonian fluid and transport of a reactive solute in a fracture-microcrack system, composed by an array of vertical microcracks connected to a main fracture (see Figure 1). Usually, microcracks are abundant in shales and are commonly arranged in subparallel arrays perpendicular to main fractures (Gale et al., 2014). The system setup is chosen, on the one hand, to capture the disparity of spatial scales between topological features in shales and, on the other, to develop and validate the multiscale algorithm for configurations that can be solved by fully resolved simulations and analytical solutions. In the modeling, both the main fracture and the microcracks are resolved explicitly; that is, pore-scale equations are solved to describe the flow and reactive transport. Single-phase flow is described by the incompressible Navier-Stokes equations:

$$\nabla \cdot \mathbf{u} = 0, \tag{1a}$$

$$\frac{\partial \mathbf{u}}{\partial t} + (\mathbf{u} \cdot \nabla)\mathbf{u} - \nu \nabla^2 \mathbf{u} = -\frac{\nabla p}{\rho}, \tag{1b}$$

where $\mathbf{u}(\mathbf{x}, t) = (u(\mathbf{x}, t), v(\mathbf{x}, t), w(\mathbf{x}, t))$, $p(\mathbf{x}, t)$, ρ, and ν are the fluid's velocity, pressure, density, and kinematic viscosity, respectively. Equation (1) are subject to the no-slip boundary condition at the fluid-solid interfaces and the following initial conditions:

$$\mathbf{u}(\mathbf{x}, t = 0) = 0, \tag{2a}$$

$$p(\mathbf{x}, t = 0) = 0. \tag{2b}$$

Solute transport is described by the advection-diffusion equation:

$$\frac{\partial c}{\partial t} = D\nabla^2 c - \nabla \cdot (\mathbf{u}c), \tag{3}$$

where c and D are the concentration and diffusivity of the solute, respectively. Equation (3) is subject to the following initial condition:

$$c(\mathbf{x}, t = 0) = 0. \tag{4}$$

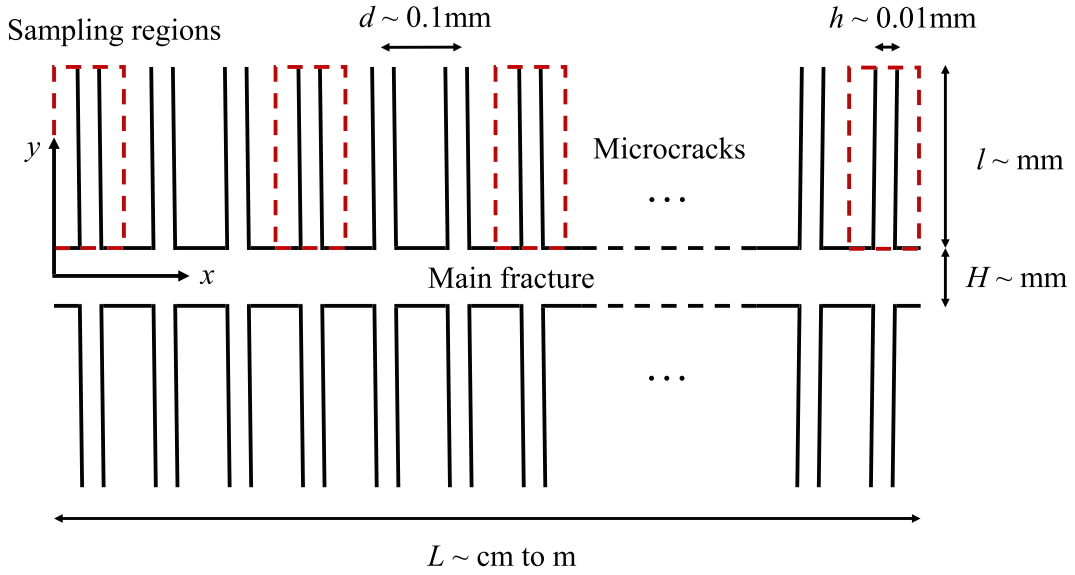

Figure 1. A schematic representation of the fracture system, where parallel microcracks are connected perpendicularly to a main fracture. The red rectangles are the sampling regions in the patch-based algorithm.

The solute undergoes a heterogenous reaction at the fluid-solid interfaces described by a Robin boundary condition applied at the walls of the microcracks:

$$-\mathbf{n} \cdot D\nabla c = K_c c, \tag{5}$$

where K_c is the reaction rate constant on the walls of the microcracks and $\mathbf{n}$ is the unit normal vector pointing from fluid to solid. Since the microcracks have much larger fluid-solid interface than the main fracture, most reaction occurs in the microcracks. Without loss of generality, we therefore assume that the reaction rate constant in the main fracture K_f is 0. Here the reaction is described by a first-order reaction model equation (5) (Li et al., 2008; Yap et al., 2013). Although the geochemistry in shales is much more complex, a first-order reaction model is adopted to test and validate the multiscale algorithm: Linear first-order reactions have been widely adopted to model fracture clogging and dissolution in the literature (Ge et al., 2012; Kang et al., 2003), as well as to test new algorithms for reactive transport in porous media (Soulaine & Tchelepi, 2016; Soulaine et al., 2017).

We start constructing the patch-based algorithm by assuming that microcracks aperture alterations due to precipitation and dissolution are negligible; then the algorithm is generalized to include the aperture alterations (section 3). It is worth emphasizing that without aperture alterations, the microcracks can also be modeled by classical upscaling methods (Arshadi & Rajaram, 2019; Lichtner & Kang, 2007; Molins et al., 2019). The patch-based algorithm is developed primarily to tackle the microcrack clogging problem.

3. Patch-Based Interpolation Algorithm

Due to the generally high density of microcracks, direct solution of the system of equations (1)–(5) is computationally prohibitive. Here we propose a two-way coupled multiscale algorithm capable of handling the length scale hierarchy at a fraction of the computational cost of fully resolved simulations. It is worth emphasizing that here "multiscale" refers to the multiscale grid resolution in different simulation domains, while the governing equations in the two different subdomains are both pore-scale equations.

We start by considering only half of the domain since the system is symmetric. The algorithm is based on the selection of several sampling regions (the red rectangles in Figure 1) along the main fracture, each containing one microcrack. Without loss of generality, the sampling regions are uniformly distributed along the fracture. Flow and reactive transport are solved only in the main fracture and the sampling regions, while the microcracks in the gaps between the sampling regions are determined by interpolation. Flow and transport in the main fracture and the microcracks are computed separately but coupled together through boundary

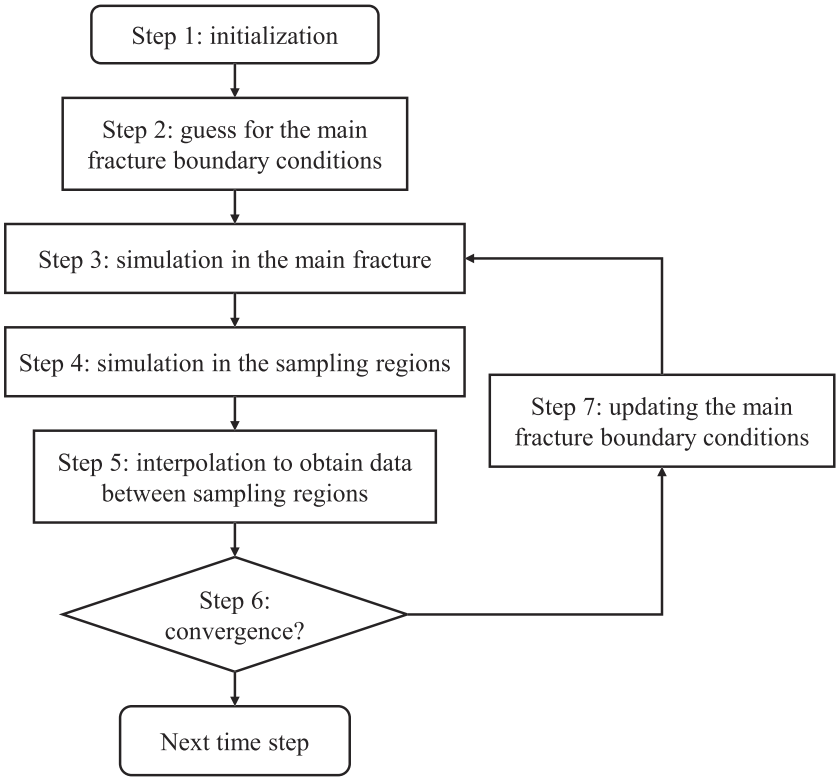

Figure 2. The flowchart of the patch-based algorithm.

conditions using a top-down/bottom-up approach. Specifically, the main fracture provides Dirichlet boundary conditions for the microcracks, while the mass flux at the microcracks inlet is modeled as a Neumann wall boundary condition for the main fracture.

The patch-based algorithm implicitly solves for the velocity, pressure, and concentration fields at t^{n+1} using the information at t^n, according to the following algorithm, schematically represented in Figure 2:

Step 1 *Initialization*. Velocity, pressure, and concentration fields at time t^n are known in the main fracture and the sampling regions.

Step 2 *Guess for the main fracture boundary conditions*. The boundary conditions at the fracture walls are initially set to

$$u_w(x, t^{n+1}) = u_w(x, t^n), \tag{6a}$$

$$f_w(x, t^{n+1}) = f_w(x, t^n), \tag{6b}$$

where u_w and f_w are the velocity and the diffusive flux at the wall boundary of the main fracture, which are later updated by the superficial averages of velocity and diffusive flux at the wall boundary (equation (9)). They represent the leakage from the main fracture to the microcracks. Specifically, f_w is determined by

$$f_w = -D\left(\frac{\partial c}{\partial y}\right)_{wall}. \tag{7}$$

Step 3 *Evolution of flow and transport in the main fracture*. March the governing equations (1a)–(3) in the main fracture, subject to the boundary conditions equation (6), from t^n to t^{n+1}, and determine pressure and concentration fields at t^{n+1} in the main fracture, that is, $p(\mathbf{x}, t^{n+1})$ and $c(\mathbf{x}, t^{n+1})$.

Step 4 *Evolution of flow and transport in the sampling regions*. Step 3 allows one to determine the distribution of pressure and concentration along the main fracture walls, and, consequently, at the inlet of the sampling regions. Wall pressure $p_w(x_m, t^{n+1})$ and concentration $c_w(x_m, t^{n+1})$ at the inlet of each

sampling region, where x_m is the position of the mth sampling region, are used as the boundary conditions. The governing equations (1a)–(3) are then marched in each sampling region from t^n to t^{n+1}, and the velocity and concentration fields at t^{n+1}, $\mathbf{u}(\mathbf{x}, t^{n+1})$, and $c(\mathbf{x}, t^{n+1})$ are solved in the mth sampling region.

Step 5 *Interpolation.* The superficial averages of the velocity and diffusive flux at the lower bound of the mth sampling region are

$$\bar{u}_m = \frac{1}{d}\int_{x_m-h/2}^{x_m+h/2} u_y(x, y = H/2, t^{n+1})dx, \tag{8a}$$

$$\bar{f}_m = \frac{1}{d}\int_{x_m-h/2}^{x_m+h/2} -D\frac{\partial c}{\partial y}(x, y = H/2, t^{n+1})dx, \tag{8b}$$

where h and d are the microcrack aperture and the center-to-center distance between adjacent microcracks, respectively. The boundary conditions along the main fracture are estimated using the following interpolation:

$$u_w^{new}(x, t^{n+1}) = \alpha_p \bar{u}_{m+1} + (1-\alpha_p)\bar{u}_m, \tag{9a}$$

$$\alpha_p = \frac{p_w(x, t^{n+1}) - p_w(x_m, t^{n+1})}{p_w(x_{m+1}, t^{n+1}) - p_w(x_m, t^{n+1})}, \tag{9b}$$

$$f_w^{new}(x, t^{n+1}) = \alpha_c \bar{f}_{m+1} + (1-\alpha_c)\bar{f}_m, \tag{9c}$$

$$\alpha_c = \frac{c_w(x, t^{n+1}) - c_w(x_m, t^{n+1})}{c_w(x_{m+1}, t^{n+1}) - c_w(x_m, t^{n+1})}. \tag{9d}$$

It is worth emphasizing that the interpolation is not based on the location but on the pressure and concentration values, which induce the velocity and diffusive flux, respectively. If $p_w(x_{m+1}, t^{n+1}) = p_w(x_m, t^{n+1})$ or $c_w(x_{m+1}, t^{n+1}) = c_w(x_m, t^{n+1})$, we set $u_w^{new}(x, t^{n+1}) = \bar{u}_m$ or $f_w^{new}(x, t^{n+1}) = \bar{f}_m$ correspondingly, to prevent the denominator from approaching zero.

Step 6 *Convergence check.* Select an acceptable tolerance ε. Define $u_w^{old}(x, t^{n+1})$ and $f_w^{old}(x, t^{n+1})$ as $u_w(x, t^{n+1})$ and $f_w(x, t^{n+1})$ from Step 3, respectively. If the convergence criterion,

$$\frac{\max_{0<x<L}|u_w^{new}(x, t^{n+1}) - u_w^{old}(x, t^{n+1})|}{\max_{0<x<L}|u_w^{new}(x, t^{n+1})|} < \varepsilon, \tag{10a}$$

$$\frac{\max_{0<x<L}|f_w^{new}(x, t^{n+1}) - f_w^{old}(x, t^{n+1})|}{\max_{0<x<L}|f_w^{new}(x, t^{n+1})|} < \varepsilon, \tag{10b}$$

is not satisfied, go to Step 7. If equation (10) is satisfied go to the next time step. We set $\varepsilon = 0.01$ in the following simulations.

Step 7 *Updating the wall boundary condition for the main fracture.* Update the wall boundary conditions as follows:

$$u_w(x, t^{n+1}) = \frac{1}{2}[u_w^{new}(x, t^{n+1}) + u_w^{old}(x, t^{n+1})], \tag{11a}$$

$$f_w(x, t^{n+1}) = \frac{1}{2}[f_w^{new}(x, t^{n+1}) + f_w^{old}(x, t^{n+1})], \tag{11b}$$

where a relaxation factor of $\frac{1}{2}$ is introduced to improve convergence. Go to Step 3.

The algorithm can be generalized to include microcrack alterations due to clogging as follows. After the concentration field at time t^{n+1} is obtained, the average concentration between t^n and t^{n+1} is determined as

$$c_{avg}(\mathbf{x}) = \frac{1}{2}[c(\mathbf{x}, t^n) + c(\mathbf{x}, t^{n+1})]. \tag{12}$$

Table 1
Geometric Parameters of the Fracture System

Geometric parameters	Length (mm)
Main fracture length (L)	30
Main fracture aperture (H)	1
Microcrack length (l)	3
Microcrack aperture (h)	0.01
Distance between microcracks (d)	0.1

We assume that in each microcrack, the precipitation does not significantly change the normal direction of the wall boundaries and the concentration variation in the normal direction is negligible. These assumptions are reasonable because the microcracks have very small aperture. Under these assumptions, the increase of the precipitate thickness in one time step is

$$\Delta s(y) = K_c c_{avg}(y) V \Delta t, \tag{13}$$

where V is the molar volume of the precipitate and y represents the position along a microcrack.

To capture the microcrack aperture alteration, we first compute a thickness profile in each sampling region using equation (13). If the thickness profile indicates the microcrack is fully clogged at its inlet, that is, $s(y = 0) \geq h/2$, no simulation will be further performed in the corresponding sampling region, and $\bar{u}_m$ and $\bar{f}_m$ in equation (8) will be permanently set to zero. If not, the sampling regions are remeshed so that the wall boundaries can match the thickness profile. The flow and transport simulation at Step 4 are to be performed in the remeshed grid in the next time step, and the microcrack aperture h in equation (9) at Step 5 is the aperture at the microcrack inlet. It is worth emphasizing that equation (13) models continuous film deposition due to precipitation (Li et al., 2008; Starchenko et al., 2016; Yap et al., 2013). Yet, in real cases, precipitation could be more localized and lead to complex precipitation patterns. In such cases, pore-scale solvers that are better suited to model complex surface evolution could be used in the sampling regions within the same patch-based framework. One such method is the smoothed particle hydrodynamics (Tartakovsky et al., 2007), which has been successfully adopted both in the context of surface precipitation problems and multiscale algorithms (Kulkarni et al., 2013).

With the patch-based algorithm, the computational cost is greatly reduced by performing simulations only in the sampling regions rather than in the entire domain. Moreover, the simulations in the sampling regions are independent, so parallel computation can be easily implemented. The patch-based algorithm can be also generalized to more complex microcracks arrangements (e.g., with variable density), or to microcracks embedded in porous media, as long as the structural variations along the main fracture are smooth enough that the quantities of interest can be evaluated by interpolation in the gaps between the sampling regions. In the following, we proceed by validating the algorithm and assessing its performance for three different transport cases: pure diffusion (section 4.1), advection and diffusion (section 4.2), and reactive transport with and without microcrack geometry alterations (section 4.3).

4. Results

The patch-based algorithm, introduced above, is implemented in OpenFoam and validated against both analytical solutions, whenever available, and fully resolved simulations under different conditions. The PIMPLE algorithm is employed to solve the incompressible Navier-Stokes equation (1), and the advection-diffusion equation is marched concurrently once the velocity field is computed. The time step is set to be small enough to ensure time step independence. The geometric parameters are chosen in line with characteristic length scales of lab-scale measurements. Specifically, aperture, length, and distance of the microcracks are chosen based on micro-CT images (Li et al., 2018), while the aperture and length of the main fracture are chosen based on core-scale measurements (Paukert Vankeuren et al., 2017). A full list of parameters is provided in Table 1. For the validation, we set the number of microcracks to 600, of which only the upper 300 are included

Table 2
Simulation Parameters for the Three Cases

Physical parameters	Value
Diffusivity (D, m^2/s)	1×10^{-9}
Kinematic viscosity (ν, m^2/s)	1×10^{-8}
Concentration at the main fracture inlet (c_{in}, [C])	1
Case 1: Pure diffusion	
Time step (δt, s)	100
Time domain	[0, 50,000 s]
Case 2: Advection-diffusion	
Time step in stage 1 (δt_1, s)	0.1
Time step in stage 2 (δt_2, s)	10
Time domain in stage 1	[0, 100 s]
Time domain in stage 2	[100, 5,000 s]
Case 3: Advection-reaction-diffusion	
Time step in stage 1 (δt_1, s)	0.1
Time step in stage 2 (δt_2, s)	10
Time domain in stage 1	[0, 100 s]
Time domain in stage 2	[100, 1×10^5 s]
Pressure boundary (p_1/ρ, m^2/s^2)	1×10^{-8}
Péclet number (Pe)	83.33
Molar volume of the precipitate (V, [1/C])	0.1

in the simulation. The grid resolution is 300×10 in the main fracture and 10×300 in the microcracks (x-y direction).

4.1. Pure Diffusion

We start by considering transport in the fracture-microcrack system by pure diffusion only. Equations (3) and (5), where $\mathbf{u} \equiv \mathbf{0}$ and $K_c = 0$, are subject to the following initial and boundary conditions:

$$c(\mathbf{x}, t = 0) = 0, \tag{14a}$$

$$c(x = 0, y, t) = 1, \tag{14b}$$

$$c(x = L, y, t) = 0, \tag{14c}$$

$$c(x, y = H/2 + l, t) = 0, \tag{14d}$$

where equations (14a), (14b), (14c), and (14d) represent the initial condition, the boundary conditions at the main fracture inlet and outlet, and the boundary condition at the microcracks outlet, respectively. Equation (3) is solved by both the proposed algorithm and a fully resolved simulation with the same set of parameters, listed in Table 2. In the following patch-based simulations, the number of sampling regions is $N = 20$, unless otherwise stated. We emphasize that the diffusivity is chosen according to the diffusivities of common ions present in hydraulic fracturing fluid. The simulations are performed on Intel Xeon Gold 6310 processor (2.1 GHz). For the set of parameters investigated here, the patch-based simulation run serially was over 10 times faster (528 s) than the fully resolved simulation (5,602 s). The computational speedup can be further increased if more microcracks, for the same number of sampling regions, are included and the code is parallelized.

Figure 3 shows the snapshots of the concentration along the centerline in the main fracture in terms of the dimensionless time $\hat{t}$:

$$\hat{t} = \frac{tD}{H}. \tag{15}$$

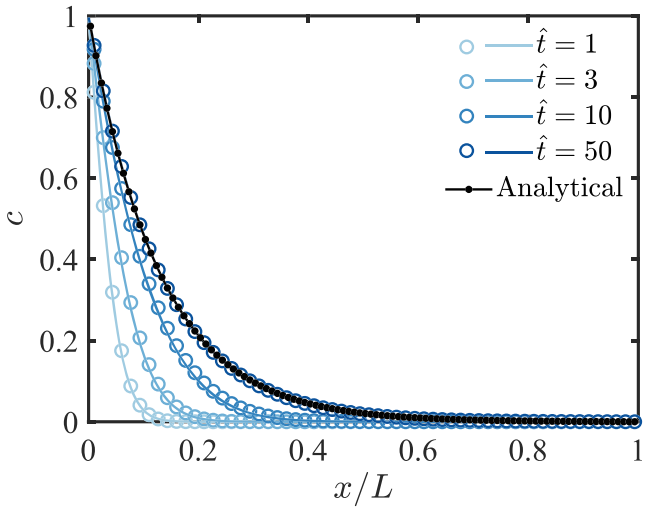

Figure 3. Temporal snapshots of the concentration at the centerline of the main fracture in the pure diffusion problem, computed by the patch-based simulation (o) and the fully resolved simulation (solid line). The dotted line is the analytical solution at steady state.

The patch-based simulation agrees well with the fully resolved simulation in the entire space and time domain, as well as with the analytical solution at the steady state (see Appendix A for the derivation):

$$\bar{c} = \frac{\sinh[(L-x)\sqrt{2h/(Hld)}]}{\sinh[L\sqrt{2h/(Hld)}]}, \tag{16}$$

where $\bar{c}$ is the cross-averaged concentration in the main fracture. As time increases, both the patch-based and the fully resolved simulations recover the analytical solution, equation (16), which proves the accuracy of both numerical solvers.

4.2. Diffusion With Advection

The second case we analyze includes transport by diffusion and advection, and equations (1), (3), and (5), where $K_c = 0$, are now subject to the following initial and boundary conditions:

$$p(\mathbf{x}, t = 0) = 0, \quad c(\mathbf{x}, t = 0) = 0, \tag{17a}$$

$$p(x = 0, y, t) = p_1, \quad c(x = 0, y, t) = 1, \tag{17b}$$

$$p(x = L, y, t) = 0, \quad c(x = L, y, t) = 0, \tag{17c}$$

$$p(x, y = H/2 + l, t) = 0, \quad c(x, y = H/2 + l, t) = 0. \tag{17d}$$

The pressure and concentration values at the main fracture inlet are higher than those at the main fracture and microcrack outlets, to drive the flow and advective diffusion in the system. The velocity and the concentration fields are marched concurrently. Yet, since the velocity field reaches the steady state much faster than the concentration field, the simulation is divided into two stages. In the first, a small time step is adopted to capture the evolution of the velocity field. As the velocity field reaches the steady state, the time step is increased to march the concentration field and control the computational burden. The details of the time stepping, as well as other parameters relevant for the simulation, are listed in Table 2. The kinematic viscosity is set to that of water and the pressure boundary is chosen such that the residence time of the fluid

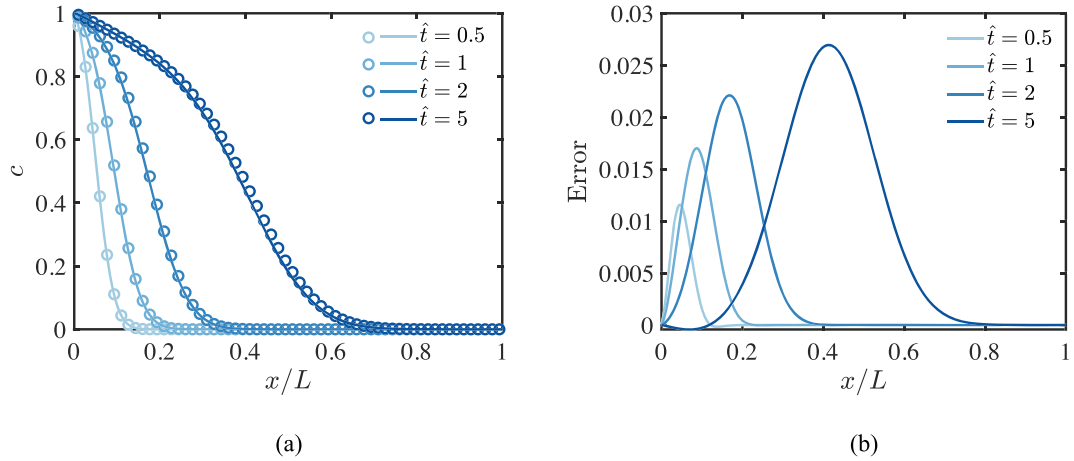

Figure 4. (a) Temporal snapshots of the concentration at the centerline of the main fracture in the advection-diffusion problem with $Pe = 83.3$, computed by the patch-based simulation (o) and the fully resolved simulation (solid line). (b) Error, that is, the normalized concentration difference, between the patch-based simulation and the fully resolved simulation.

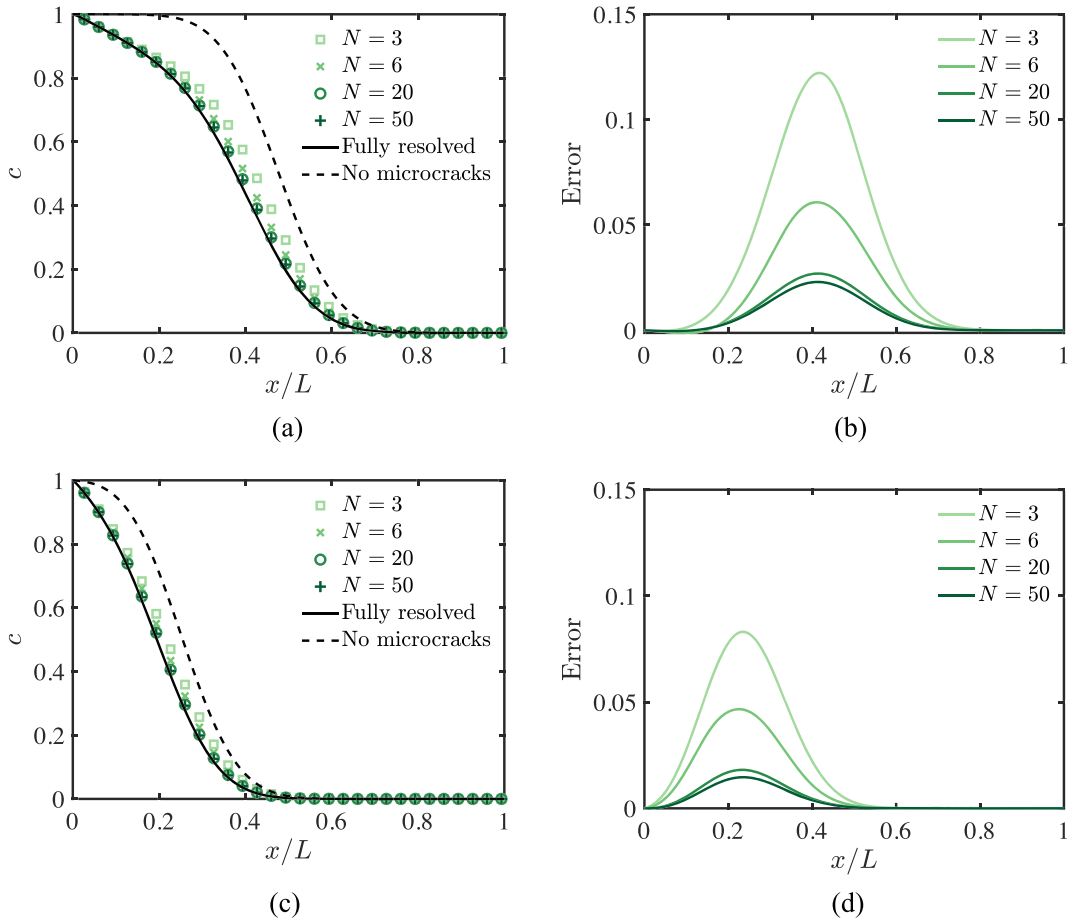

Figure 5. (a and c) Snapshots of the concentration at the centerline of the main fracture in the advection-diffusion problem at $\hat{t} = 5$. The symbols are obtained by the patch-based simulation with different number of sampling regions; the solid line represents the fully resolved simulation, and the dashed line is the simulation results in the main fracture excluding the microcracks: (a) $Pe = 83.3$; (c) $Pe = 41.7$. (b and d) The error between the patch-based simulation and the fully resolved simulation in (a) and (c), respectively.

is similar to that of lab experiments (i.e., a few hours) (Paukert Vankeuren et al., 2017). We define the Péclet number as

$$Pe = \frac{H^2 p_1}{12\mu D}, \tag{18}$$

where μ is the dynamic viscosity. Note that Pe is defined based on the advection-diffusion in the main fracture. In the microcracks, the maximum velocity is about 1/1,000 the maximum velocity in the main fracture; that is, the mean flow through the microcracks is small but nonzero. The Péclet number in the microcracks is much smaller than 1; that is, mass transport is controlled by diffusion, and the fluid loss through the microcracks is less than 1%, consistent with lab-scale measurements. Figure 4a shows the centerline concentration snapshots at different times for $Pe = 83.3$. The results show good agreement between the patch-based and the fully resolved simulations. Figure 4b presents the error of the patch-based simulation, that is, the difference between the concentration in the patch-based and the fully resolved simulations, normalized by the inlet concentration in the main fracture. The maximum error generally locates where the concentration gradient is the largest, since the interpolation becomes less accurate in the presence of sharp concentration drops.

Next, the influence of Pe and the number of sampling regions N is investigated. Figure 5a shows the simulation results at $\hat{t} = 5$ for $Pe = 83.3$. Symbols represent the patch-based simulations with different number of sampling regions N. As N increases, the results from the patch-based algorithm converge to the fully resolved simulation, and the error between them decreases (Figure 5b). The convergence can also be used

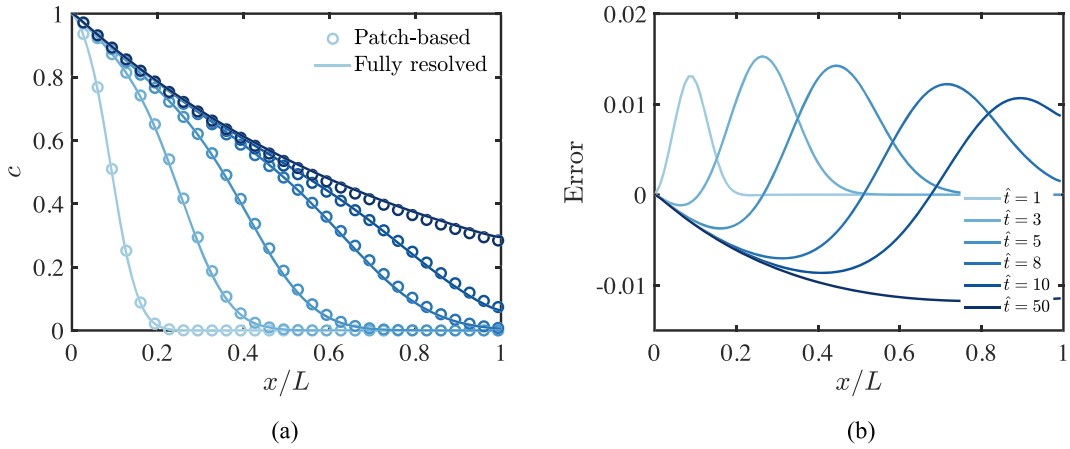

Figure 6. (a) Temporal snapshots of the concentration at the centerline of the main fracture in the advection-diffusion-reaction problem at $\hat{t} = 1, 3, 5, 8, 10, 50$ (from light color to dark color). (b) Error, that is, the normalized concentration difference, between the patch-based simulation and the fully resolved simulation.

to determine the required number of sampling regions when fully resolved simulations are computationally prohibitive. The dashed line in Figure 5a represents the simulation results in the main fracture excluding the microcracks and allows one to quantitatively assess the contribution of the microcracks to transport. Even with only a few sampling regions, the contribution of the microcracks can be roughly captured. Figures 5c and 5d represent the same simulations but with $Pe = 41.7$. The concentration front moves slower as Pe decreases because of the weaker advection, and the error of the patch-based method also decreases.

4.3. Reactive Transport

In the reactive transport scenario, the equations (1), (3), and (5) are subjected to the following initial and boundary conditions:

$$p(\mathbf{x}, t = 0) = 0, \quad c(\mathbf{x}, t = 0) = 0, \tag{19a}$$

$$p(x = 0, y, t) = p_1, \quad c(x = 0, y, t) = 1, \tag{19b}$$

$$p(x = L, y, t) = 0, \quad \left.\frac{\partial c}{\partial x}\right|_{x=L} = 0, \tag{19c}$$

$$p(x, y = H/2 + l, t) = 0, \quad \left.\frac{\partial c}{\partial y}\right|_{y=H/2+l} = 0. \tag{19d}$$

The boundary conditions are similar to those of section 4.2 with the only difference that zero gradient concentration boundaries are applied at the outlets of the main fracture and microcracks. In addition, a nonzero reaction rate constant K_c is introduced in equation (5) for the microcracks. The reaction rate K_c walls is selected so that solute breakthrough can be observed at the main fracture outlet, which is usually measured in laboratory measurements. As previously discussed in section 2, reaction on the walls of the main fracture is neglected due to the small interfacial area (i.e., $K_f = 0$). The Damköhler number, the ratio between diffusive to reactive time scales, is defined as

$$Da = \frac{K_c H}{D}. \tag{20}$$

Figure 6a shows the concentration snapshots at six selected times with $Da = 2 \times 10^{-3}$, including concentration profiles at the breakthrough ($\hat{t} = 8$), after the breakthrough ($\hat{t} = 10$) and at the steady state ($\hat{t} = 50$). Good agreement is observed between the patch-based simulation and the fully resolved simulation. The error, plotted in Figure 6b, does not continuously increase with time as that of Figure 4b, since the system finally reaches steady state. The speedup gain of the patch-based algorithm is again significant: The total computational time is 4,751 s for the patch-based simulation (without parallel computation) and 36,490 s for the fully resolved simulation.

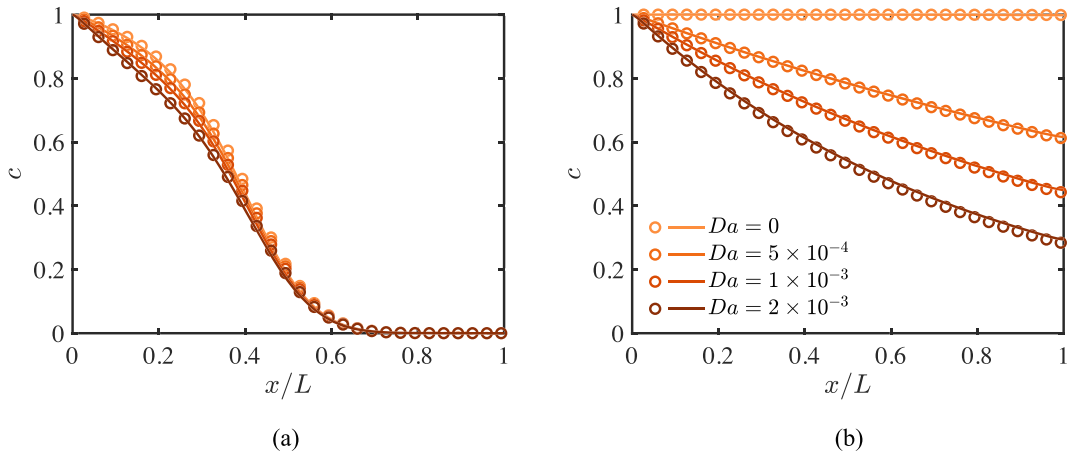

Figure 7. Concentration profiles at the centerline of the main fracture in the advection-diffusion-reaction problem, computed by the patch-based simulation (o) and the fully resolved simulation (solid line): (a) at $\hat{t} = 5$; (b) at $\hat{t} = 50$.

Figure 7 shows the concentration profiles before (Figure 7a) and after (Figure 7b) the breakthrough for the patch-based and the fully resolved simulations at different *Da*. The good agreement suggests that the patch-based algorithm works well under different *Da*. The results also indicate that reaction rates can have a great impact on the concentration field after breakthrough, even if the difference for the concentration fields before the breakthrough is small. It takes time for the main fracture to be affected by the reaction in the microcracks, because the transport in the microcracks is dominated by diffusion, which is slower than the advective-diffusive transport in the main fracture. This implies that the impact of reaction can be significantly underestimated if only early-stage data are considered. Figure 8 shows the concentration breakthrough curves for different *Da* and the error between patch-based and fully resolved simulations. The breakthrough curve is lower when the reaction rate is higher, because more solute is consumed in the microcracks. Note that all the errors are bounded by 3.3%, which would be the upscaling error H/L if the main fracture were described by a one-dimensional advection-diffusion model rather than pore-scale equations (Pavliotis & Stuart, 2008). This suggests that the patch-based algorithm would not introduce a significant error and could be potentially implemented in setups where continuum-scale models for the main fracture are coupled to pore-scale equations for the microcracks.

Next, the microcrack aperture alteration is included in the patch-based algorithm. Figure 9 presents concentration snapshots along the centerline of the main fracture. The dashed and solid lines represent

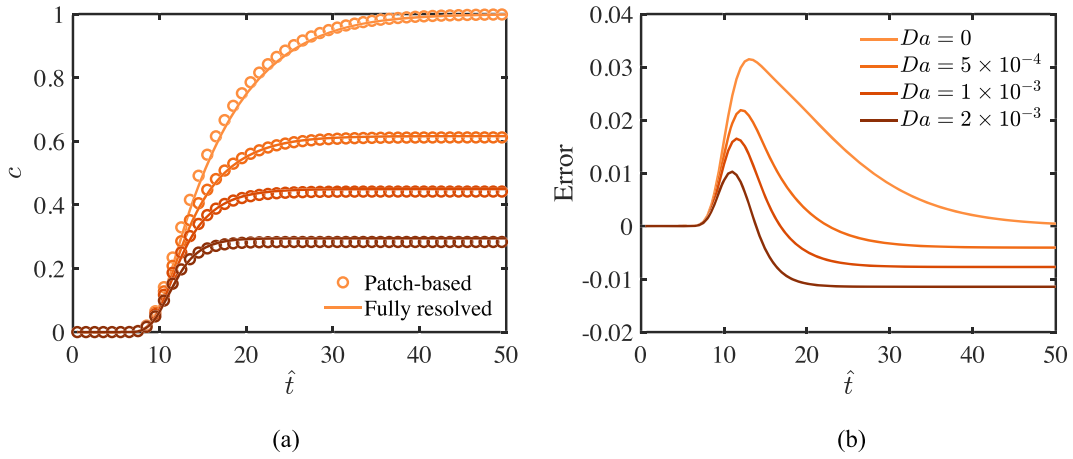

Figure 8. (a) Breakthrough curves at the center of the main fracture outlet in the advection-diffusion-reaction problem, computed by the patch-based simulation (o) and the fully resolved simulation (solid line). (b) Error, that is, the normalized concentration difference, between the patch-based simulation and the fully resolved simulation.

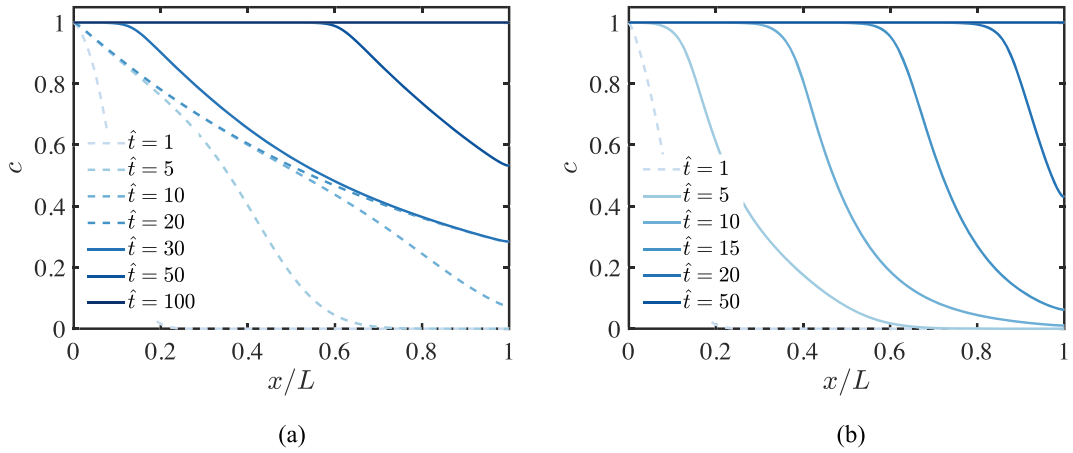

Figure 9. Temporal snapshots of the concentration at the centerline of the main fracture with microcrack clogging, computed by the patch-based simulation: (a) $Da = 0.002$ and (b) $Da = 0.02$. The dashed and solid lines represent the concentration profiles before and after the first microcrack has been fully clogged, respectively.

concentration snapshots before and after the first microcrack is fully clogged, respectively. When the reaction rate is low ($Da = 0.002$), the concentration front moves faster than the clogging; that is, microcracks get fully clogged after concentration breakthrough in the main fracture (Figure 9a). When the reaction rate is higher ($Da = 0.02$), the microcracks become fully clogged as the concentration front is moving down the main fracture (Figure 9b). Figure 10 shows the pattern of the precipitate in the fully clogged fracture located closest to the main fracture inlet, that is, the first fully clogged microcrack. The precipitate is more concentrated near the microcrack inlet when the reaction rate is higher.

Finally, in Figure 11 we plot the breakthrough curves at the main fracture outlet with microcrack alterations. When the reaction rate is small ($Da = 0.002$), the breakthrough curve has three stages: First, the concentration increases as flow and transport in the main fracture carry the solute from the inlet to the outlet; then, the concentration reaches a plateau when slow microcracks alterations have little effect on solute transport toward the main fracture outlet. Finally, concentration increases again because, as the microcracks

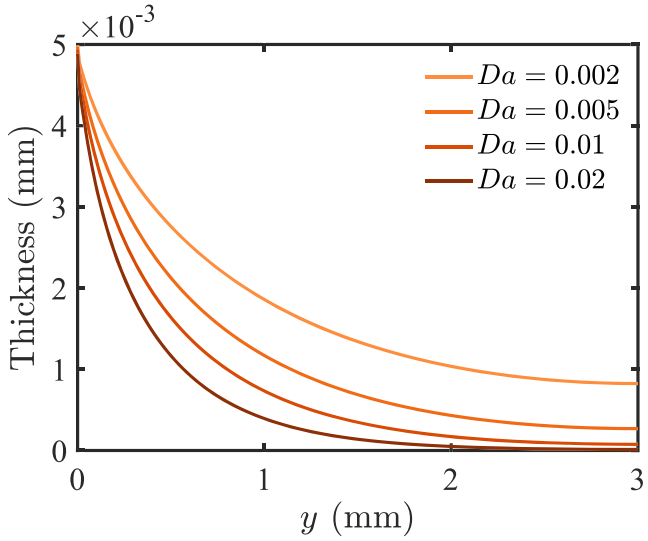

Figure 10. Thickness of precipitate along a microcrack for fully clogged conditions. The microcrack is the one closest to the main fracture inlet.

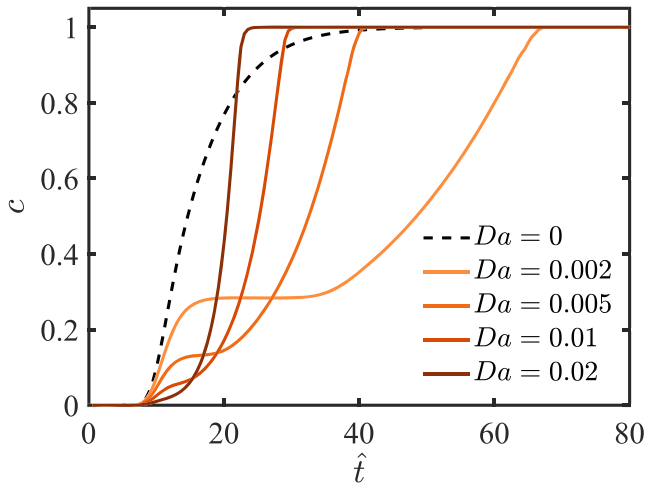

Figure 11. Breakthrough curves at the center of the main fracture outlet computed by the patch-based simulation with microcrack aperture alteration effects included.

get progressively clogged, less solute is lost into the microcracks: This leads to an increase in concentration until saturation, when all microcracks are fully clogged. For higher reaction rates, the three stages collapse into a single stage, because the microcracks become fully clogged not far behind the concentration front. In addition, compared to the nonreactive breakthrough curve (dashed line in Figure 11), saturation is reached more slowly with lower reaction rates because of slow clogging. The opposite behavior is observed for higher reaction rates.

5. Conclusions

We considered reactive transport in a multiscale fracture system, which requires microscale simulations in a macroscopic domain. A patch-based multiscale algorithm is developed, in which microscale simulations are performed in small sampling regions, while the regions outside are evaluated by interpolation. The algorithm solves flow and reactive transport implicitly and ensures a bottom-up top-down coupling. Specifically, the patch-based algorithm is applied to a setup where an array of microcracks is connected to a main fracture. The results are validated against fully resolved simulations and a steady-state analytical solution. The algorithm is generalized to include microcrack alteration due to precipitation. The major conclusions are as follows:

- the patch-based simulations agree well with the fully resolved simulations in the entire space and time domain for all the cases investigated;
- the patch-based algorithm can model the reactive transport with microcrack clogging, which cannot be accurately upscaled by traditional methods.
- the speedup of the patch-based simulations (without parallel computation) is about tenfold compared to the fully resolved simulation for the tested examples at the core scale; further improvements can be expected for parallel implementation and larger systems;
- in the pure diffusion case, both the patch-based simulation and the fully resolved simulation can recover the steady-state analytical solution, indicating the simulations are reliable.

While tested on an idealized geometry, current work includes application of the method to more complex fracture networks as well as its implementation in the context of both algorithm refinement techniques where equations at different scales are coupled together, and immersed boundary methods techniques to curtail the cost of remeshing due fracture alterations (Yousefzadeh & Battiato, 2019). Another open challenge is the treatment of multiple time scales. In realistic applications, the time step for solving equations in microcracks could be so small that the time integration in patches for the entire simulation time could be unfeasible. Current efforts involve the generalization of the patch-based algorithm to handle multiplicity of time scales as well. Future work will also include generalization of the multiscale algorithm to reaction networks, which more realistically represent shale geochemistry.

Appendix A: Analytical Solution for Pure Diffusive Transport

Consider a volume element in the main fracture between x and $x + \delta x$. The number of microcracks that are connected to the element is

$$\delta n = 2\frac{\delta x}{d}. \tag{A1}$$

At steady state, the concentration is linear in each microcrack, so the mass flow rate that leaves the volume element in the y direction (i.e., through the microcracks) is

$$\delta Q_y = \delta n D h \frac{\bar{c}}{l}. \tag{A2}$$

Here we assume the concentration in the volume element is uniform with value $\bar{c}$. The mass flow rate that leaves the volume element in the x direction is

$$\delta Q_x = -DH\frac{\partial^2 \bar{c}}{\partial x^2}\delta x. \tag{A3}$$

The mass balance equation reads as follows:

$$\delta Q_x + \delta Q_y = 0. \tag{A4}$$

Combining equations (A1) and (A4) leads to

$$\frac{\partial^2 \bar{c}}{\partial x^2} = \frac{2h}{Hld}\bar{c}, \tag{A5}$$

which is subjected to the boundary conditions

$$\bar{c}(x = 0) = 1, \quad \bar{c}(x = L) = 0, \tag{A6}$$

and whose solution for the average concentration is

$$\bar{c} = \frac{\sinh[(L - x)\sqrt{2h/(Hld)}]}{\sinh[L\sqrt{2h/(Hld)}]}. \tag{A7}$$

Acknowledgments
This work was supported as part of the Center for Mechanistic Control of Water-Hydrocarbon-Rock Interactions in Unconventional and Tight Oil Formations (CMC-UF), an Energy Frontier Research Center funded by the U.S. Department of Energy, Office of Science under DOE (BES) Award DE-SC0019165. All the synthetically generated data are available online (https://doi.org/10.4121/uuid:3f499e5e-065d-46ac-8a81-1f8976ac6542).

References

Alalli, A., Li, Q., Jew, A., Kohli, A., Bargar, J., Zoback, M., & Kovscek, A. (2018). Effects of hydraulic fracturing fluid chemistry on shale matrix permeability. In *Unconventional Resources Technology Conference* (pp. 808–817). Houston, Texas.

Arbogast, T., Pencheva, G., Wheeler, M. F., & Yotov, I. (2007). A multiscale mortar mixed finite element method. *Multiscale Modeling & Simulation*, *6*(1), 319–346.

Arshadi, M., & Rajaram, H. (2019). Transport with bimolecular reactions in a fracture-matrix system: Analytical solutions with applications to in situ chemical oxidation. *Water Resources Research*, *55*, 3904–3924. https://doi.org/10.1029/2019WR024762

Arunachalam, H., Onori, S., & Battiato, I. (2015). On veracity of macroscopic lithium-ion battery models. *Journal of The Electrochemical Society*, *162*(10), A1,940–A1,951.

Balhoff, M. T., Thomas, S. G., & Wheeler, M. F. (2008). Mortar coupling and upscaling of pore-scale models. *Computational Geosciences*, *12*(1), 15–27.

Balhoff, M. T., Thompson, K. E., & Hjortsø, M. (2007). Coupling pore-scale networks to continuum-scale models of porous media. *Computers & Geosciences*, *33*(3), 393–410.

Battiato, I., O'Malley, D., Miller, C. T., Takhar, P. S., Valdés-Parada, F. J., & Wood, B. D. (2019). Theory and applications of macroscale models in porous media. *Transport in Porous Media*, *130*, 5–76.

Battiato, I., & Tartakovsky, D. (2011). Applicability regimes for macroscopic models of reactive transport in porous media. *Journal of Contaminant Hydrology*, *120*, 18–26.

Battiato, I., Tartakovsky, D. M., Tartakovsky, A. M., & Scheibe, T. D. (2011). Hybrid models of reactive transport in porous and fractured media. *Advances in Water Resources*, *34*(9), 1140–1150.

Boso, F., & Battiato, I. (2013). Homogenizability conditions for multicomponent reactive transport. *Advances in Water Resources*, *62*, 254–265.

Dejam, M., Hassanzadeh, H., & Chen, Z. (2014). Shear dispersion in a fracture with porous walls. *Advances in Water Resources*, *74*, 14–25.

Ellsworth, W. L. (2013). Injection-induced earthquakes. *Science*, *341*(6142), 1225942.

Entrekin, S., Evans-White, M., Johnson, B., & Hagenbuch, E. (2011). Rapid expansion of natural gas development poses a threat to surface waters. *Frontiers in Ecology and the Environment*, *9*(9), 503–511.

Gale, J. F., Laubach, S. E., Olson, J. E., Eichhubl, P., & Fall, A. (2014). Natural fractures in shale: A review and new observationsnatural fractures in shale: A review and new observations. *AAPG Bulletin*, *98*(11), 2165–2216.

Ge, Q., Yap, Y., Vargas, F., Zhang, M., & Chai, J. (2012). A total concentration method for modeling of deposition. *Numerical Heat Transfer, Part B: Fundamentals*, *61*(4), 311–328.
Gear, C. W., Li, J., & Kevrekidis, I. G. (2003). The gap-tooth method in particle simulations. *Physics Letters A*, *316*(3-4), 190–195.
Gregory, K. B., Vidic, R. D., & Dzombak, D. A. (2011). Water management challenges associated with the production of shale gas by hydraulic fracturing. *Elements*, *7*(3), 181–186.
Heße, F., Radu, F. A., Thullner, M., & Attinger, S. (2009). Upscaling of the advection-diffusion-reaction equation with Monod reaction. *Advances in Water Resources*, *32*(8), 1336–1351.
Hyman, J., Painter, S. L., Viswanathan, H., Makedonska, N., & Karra, S. (2015). Influence of injection mode on transport properties in kilometer-scale three-dimensional discrete fracture networks. *Water Resources Research*, *51*, 7289–7308. https://doi.org/10.1002/2015WR017151
Kang, Q., Zhang, D., & Chen, S. (2003). Simulation of dissolution and precipitation in porous media. *Journal of Geophysical Research*, *108*(B10), 2505. https://doi.org/10.1029/2003JB002504
Karra, S., Makedonska, N., Viswanathan, H. S., Painter, S. L., & Hyman, J. D. (2015). Effect of advective flow in fractures and matrix diffusion on natural gas production. *Water Resources Research*, *51*, 8646–8657. https://doi.org/10.1002/2014WR016829
Kevrekidis, I. G., Gear, C. W., & Hummer, G. (2004). Equation-free: The computer-aided analysis of complex multiscale systems. *AIChE Journal*, *50*(7), 1346–1355.
Korneev, S., & Battiato, I. (2016). Sequential homogenization of reactive transport in polydisperse porous media. *Multiscale Modeling & Simulation*, *14*(4), 1301–1318.
Kulkarni, P. M., Fu, C.-C., Shell, M. S., & Gary Leal, L. (2013). Multiscale modeling with smoothed dissipative particle dynamics. *The Journal of Chemical Physics*, *138*(23), 234105.
Li, X., Huang, H., & Meakin, P. (2008). Level set simulation of coupled advection-diffusion and pore structure evolution due to mineral precipitation in porous media. *Water Resources Research*, *44*, W12407. https://doi.org/10.1029/2007WR006742
Li, Q., Jew, A. D., Kiss, A. M., Kohli, A., Alalli, A., Kovscek, A. R., et al. (2018). Imaging pyrite oxidation and barite precipitation in gas and oil shales. In *Unconventional Resources Technology Conference* (pp. 875–884). Houston, Texas.
Li, L., Peters, C. A., & Celia, M. A. (2006). Upscaling geochemical reaction rates using pore-scale network modeling. *Advances in Water Resources*, *29*(9), 1351–1370.
Lichtner, P. C., & Kang, Q. (2007). Upscaling pore-scale reactive transport equations using a multiscale continuum formulation. *Water Resources Research*, *43*, W12S15. https://doi.org/10.1029/2006WR005664
Liden, T., Clark, B. G., Hildenbrand, Z. L., & Schug, K. A. (2017). Unconventional oil and gas production: Waste management and the water cycle, *Advances in Chemical Pollution, Environmental Management and Protection* (Vol. 1, pp. 17–45): Elsevier.
Ling, B., Oostrom, M., Tartakovsky, A. M., & Battiato, I. (2018). Hydrodynamic dispersion in thin channels with micro-structured porous walls. *Physics of Fluids*, *30*(7), 76601.
Ling, B., Tartakovsky, A. M., & Battiato, I. (2016). Dispersion controlled by permeable surfaces: Surface properties and scaling. *Journal of Fluid Mechanics*, *801*, 13–42.
Maloney, K. O., & Yoxtheimer, D. A. (2012). Production and disposal of waste materials from gas and oil extraction from the Marcellus shale play in Pennsylvania. *Environmental Practice*, *14*(4), 278–287.
Mehmani, Y., & Balhoff, M. T. (2014). Bridging from pore to continuum: A hybrid mortar domain decomposition framework for subsurface flow and transport. *Multiscale Modeling & Simulation*, *12*(2), 667–693.
Mehmani, Y., Sun, T., Balhoff, M. T., Eichhubl, P., & Bryant, S. (2012). Multiblock pore-scale modeling and upscaling of reactive transport: Application to carbon sequestration. *Transport in Porous Media*, *95*(2), 305–326.
Middleton, R. S., Carey, JWilliam, Currier, R. P., Hyman, J. D., Kang, Q., Karra, S., et al. (2015). Shale gas and non-aqueous fracturing fluids: Opportunities and challenges for supercritical CO2. *Applied Energy*, *147*, 500–509.
Molins, S., Trebotich, D., Arora, B., Steefel, C. I., & Deng, H. (2019). Multi-scale model of reactive transport in fractured media: Diffusion limitations on rates. *Transport in Porous Media*, *128*(2), 701–721.
Moslehi, M., de Barros, F. P., Ebrahimi, F., & Sahimi, M. (2016). Upscaling of solute transport in disordered porous media by wavelet transformations. *Advances in Water Resources*, *96*, 180–189.
Orgogozo, L., Golfier, F., Buès, M., & Quintard, M. (2010). Upscaling of transport processes in porous media with biofilms in non-equilibrium conditions. *Advances in Water Resources*, *33*(5), 585–600.
Paukert Vankeuren, A. N., Hakala, A. J., Jarvis, K., & Moore, J. E. (2017). Mineral reactions in shale gas reservoirs: Barite scale formation from reusing produced water as hydraulic fracturing fluid. *Environmental Science & Technology*, *51*(16), 9391–9402.
Pavliotis, G., & Stuart, A. (2008). *Multiscale methods: Averaging and homogenization*. New York: Springer Science & Business Media.
Peszyńska, M., Wheeler, M. F., & Yotov, I. (2002). Mortar upscaling for multiphase flow in porous media. *Computational Geosciences*, *6*(1), 73–100.
Picchi, D., & Battiato, I. (2018). The impact of pore-scale flow regimes on upscaling of immiscible two-phase flow in porous media. *Water Resources Research*, *54*, 6683–6707. https://doi.org/10.1029/2018WR023172
Picchi, D., & Battiato, I. (2019). Relative permeability scaling from pore-scale flow regimes. *Water Resources Research*, *55*, 3215–3233. https://doi.org/10.1029/2018WR024251
Picchi, D., Ullmann, A., & Brauner, N. (2018). Modeling of core-annular and plug flows of newtonian/non-newtonian shear-thinning fluids in pipes and capillary tubes. *International Journal of Multiphase Flow*, *103*, 43–60.
Rosa, L., Rulli, M. C., Davis, K. F., & D'Odorico, P. (2018). The water-energy nexus of hydraulic fracturing: A global hydrologic analysis for shale oil and gas extraction. *Earth's Future*, *6*, 745–756.
Roubinet, D., de Dreuzy, J.-R., & Tartakovsky, D. M. (2012). Semi-analytical solutions for solute transport and exchange in fractured porous media. *Water Resources Research*, *48*, W01542. https://doi.org/10.1029/2011WR011168
Roubinet, D., & Tartakovsky, D. M. (2013). Hybrid modeling of heterogeneous geochemical reactions in fractured porous media. *Water Resources Research*, *49*, 7945–7956. https://doi.org/10.1002/2013WR013999
Sakmar, S. L. (2011). Shale gas development in North America: An overview of the regulatory and environmental challenges facing the industry. In *North American unconventional gas conference and exhibition* (pp. 144279). Society of Petroleum Engineers.
Samaey, G., Roberts, A. J., & Kevrekidis, I. G. (2010). *Multiscale methods: Bridging the scales in science and engineering Edited by* F. Jacob. Oxford: Oxford Scholarship Online.
Soulaine, C., Roman, S., Kovscek, A., & Tchelepi, H. A. (2017). Mineral dissolution and wormholing from a pore-scale perspective. *Journal of Fluid Mechanics*, *827*, 457–483.
Soulaine, C., & Tchelepi, H. A. (2016). Micro-continuum approach for pore-scale simulation of subsurface processes. *Transport in Porous Media*, *113*(3), 431–456.

Starchenko, V., Marra, C. J., & Ladd, A. J. (2016). Three-dimensional simulations of fracture dissolution. *Journal of Geophysical Research: Solid Earth*, *121*, 6421–6444. https://doi.org/10.1002/2016JB013321

Takhar, P. S., Maier, D. E., Campanella, O. H., & Chen, G. (2011). Hybrid mixture theory based moisture transport and stress development in corn kernels during drying: Validation and simulation results. *Journal of Food Engineering*, *106*(4), 275–282.

Tartakovsky, A. M., Meakin, P., Scheibe, T. D., & Eichiler West, R. M. (2007). Simulations of reactive transport and precipitation with smoothed particle hydrodynamics. *Journal of Computational Physics*, *222*(2), 654–672.

Tartakovsky, A. M., Tartakovsky, D. M., Scheibe, T. D., & Meakin, P. (2008). Hybrid simulations of reaction-diffusion systems in porous media. *SIAM Journal on Scientific Computing*, *30*(6), 2799–2816.

Torres, L., Yadav, O. P., & Khan, E. (2016). A review on risk assessment techniques for hydraulic fracturing water and produced water management implemented in onshore unconventional oil and gas production. *Science of the Total Environment*, *539*, 478–493.

Vengosh, A., Jackson, R. B., Warner, N., Darrah, T. H., & Kondash, A. (2014). A critical review of the risks to water resources from unconventional shale gas development and hydraulic fracturing in the United States. *Environmental Science & Technology*, *48*(15), 8334–8348.

Vidic, R. D., Brantley, S. L., Vandenbossche, J. M., Yoxtheimer, D., & Abad, J. D. (2013). Impact of shale gas development on regional water quality. *Science*, *340*(6134), 1235009.

Wang, Z., Guo, Y., & Wang, M. (2016). Permeability of high-Kn real gas flow in shale and production prediction by pore-scale modeling. *Journal of Natural Gas Science and Engineering*, *28*, 328–337.

Wang, Z., Wang, M., & Chen, S. (2018). Coupling of high Knudsen number and non-ideal gas effects in microporous media. *Journal of Fluid Mechanics*, *840*, 56–73.

Weinan, E., Engquist, B., Li, X., Ren, W., & Vanden-Eijnden, E. (2007). Heterogeneous multiscale methods: A review. *Communications in Computational Physics*, *2*(3), 367–450.

Yap, Y., Vargas, F., & Chai, J. (2013). A level-set method for convective-diffusive particle deposition. *Applied Mathematical Modelling*, *37*(7), 5245–5259.

Yousefzadeh, M., & Battiato, I. (2017). Physics-based hybrid method for multiscale transport in porous media. *Journal of Computational Physics*, *344*, 320–338.

Yousefzadeh, M., & Battiato, I. (2019). High order ghost-cell immersed boundary method for generalized boundary conditions. *International Journal of Heat and Mass Transfer*, *137*, 585–598.